Supplementary Information for:

Single-molecule fluorescence spectroscopy maps the folding landscape of a large protein

Menahem Pirchi[1,*], Guy Ziv[1,*,&], Inbal Riven[1], Sharona Sedghani Cohen[1], Nir Zohar[1]

Yoav Barak[2] and Gilad Haran[1]

[1]Chemical Physics Department and [2]Chemical Research Support, Weizmann Institute of Science, Rehovot 76100, Israel

Supplementary Figures

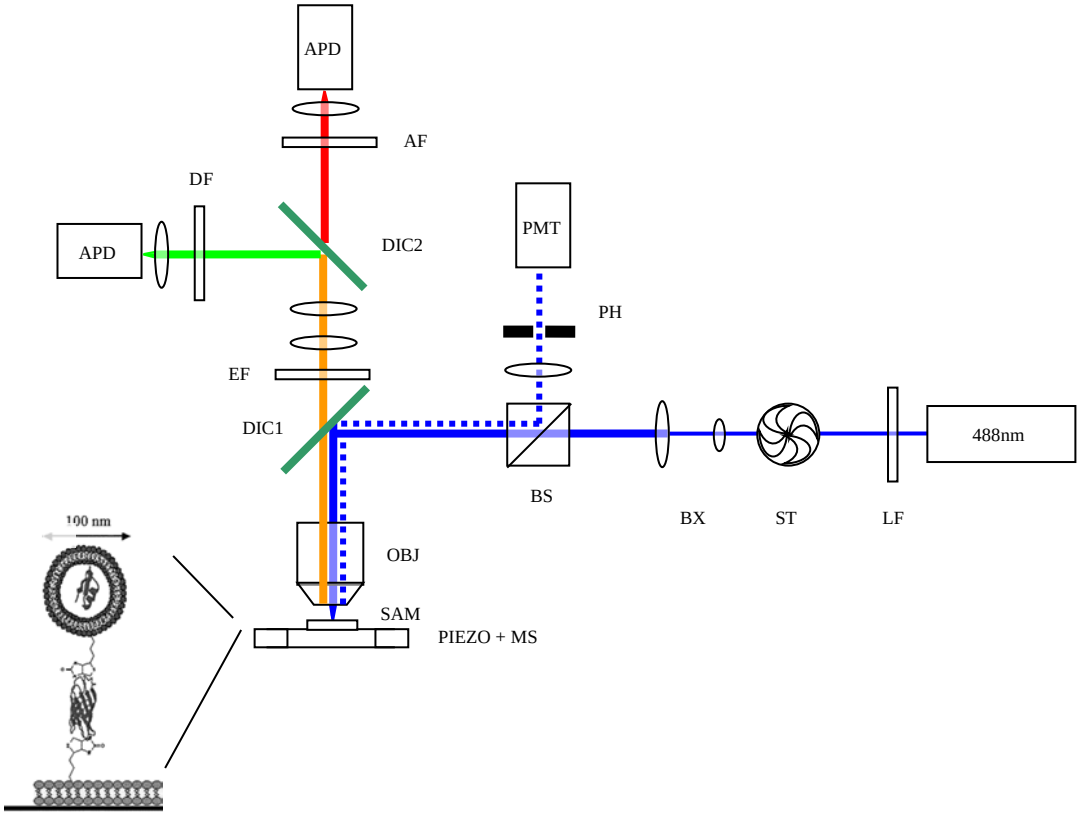

Figure S1. Schematic representation of the high-throughput SM apparatus. For description, including designation of the various parts designated in the figure, see the Supplementary Methods section.

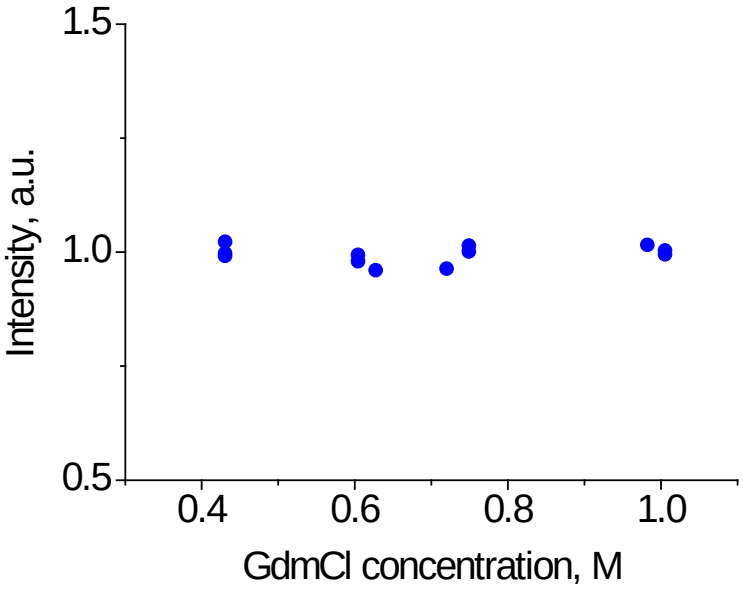

Figure S2. **Acceptor emission intensity as a function of GdmCl concentration**. Double-labeled protein samples at various concentrations of the denaturant were excited at 560 nm and the acceptor emission was measured. For details see the Supplementary Methods section.

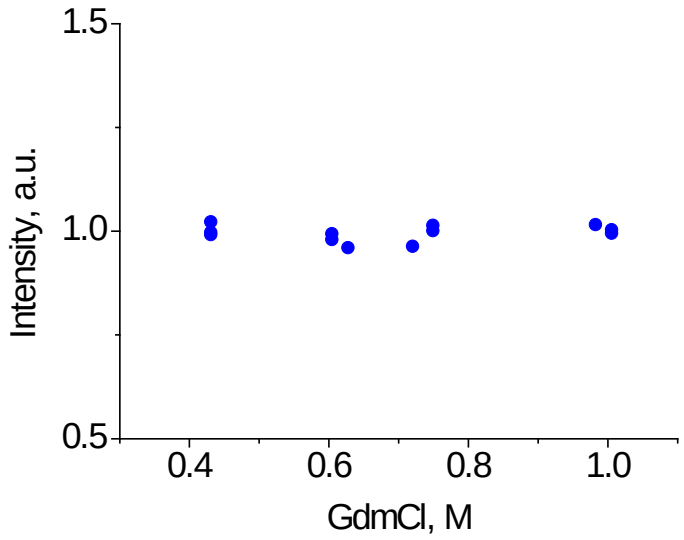

Figure S3. **γ-corrected total emission intensity as function of GdmCl concentration.** For details see the Supplementary Methods section.

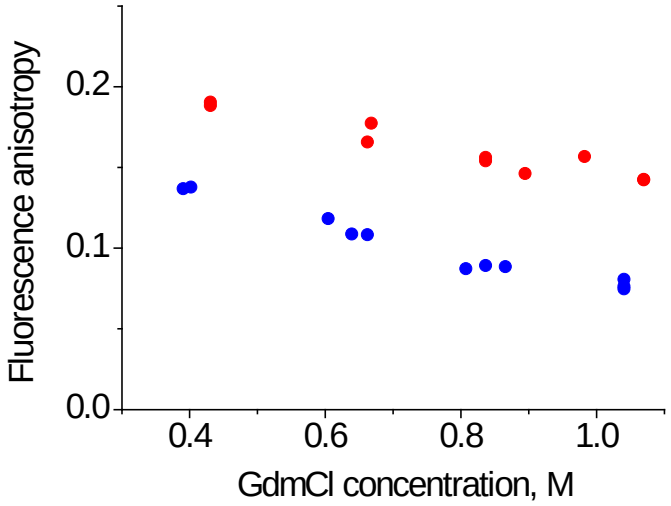

Figure S4. **Fluorescence anisotropy as function of GdmCl concentration.** Blue dots are the measured values for donor-only-protein molecules excited at 465 nm. Red dots are measured values of double-labeled protein molecules excited at 560 nm. For details see the Supplementary Methods section.

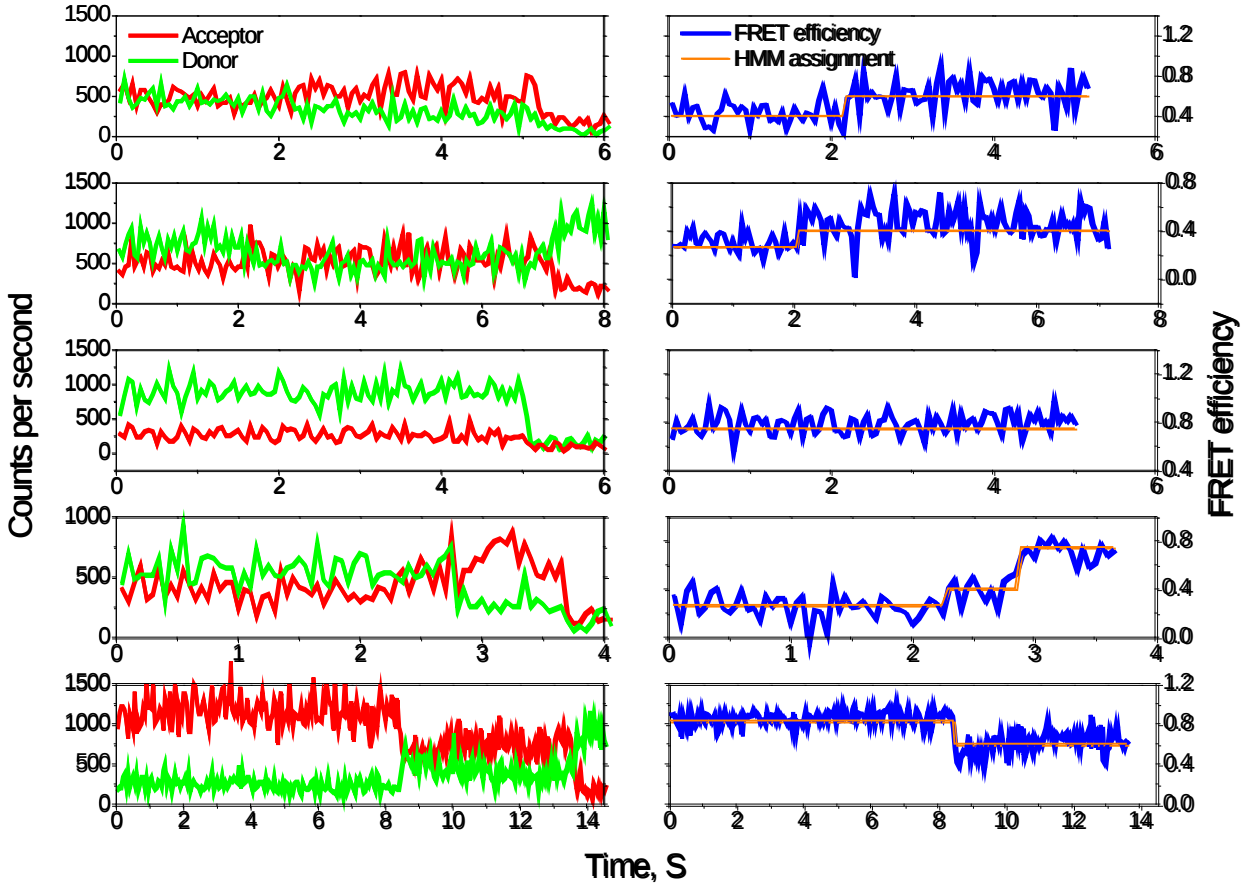

Figure S5. **Additional single-molecule FRET trajectories.** In each example the left panel shows the experimental traces from the donor and acceptor channels, while the right panel shows the FRET efficiency trace, calculated till the photobleaching point. The transitions between different FRET states seen in the trajectories are anti-correlated, as were >90% of the transitions seen in our data. The orange lines in the right panels are state assignments based on the HMM analysis, and obtained with the Viterbi algorithm.

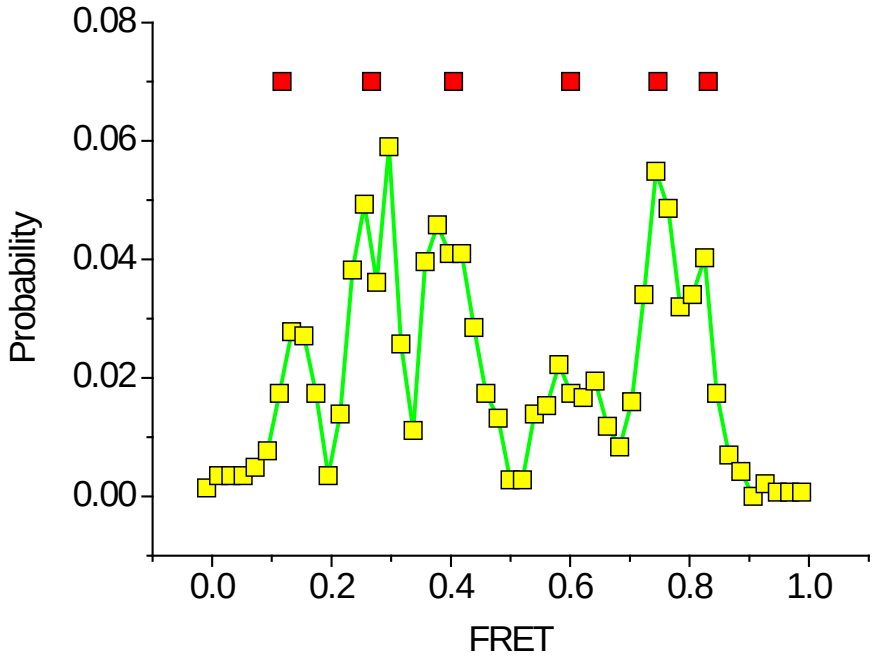

Figure S6. Histogram constructed from trajectory segments. Single-molecule trajectories were segmented using the Viterbi algorithm, based on the HMM parameters. Average FRET efficiency values were calculated for segments longer than 1 second, and were used to generate the histogram (yellow symbols connected by a green line). Red symbols designate positions of FRET states as predicted by the HMM analysis. A similar histogram constructed following random segmentation of the data did not show the peak sub-structure. This figure serves as a consistency check for the HMM analysis, and shows the validity of the representation of the data with six states.

Table S1. Statistics of data sets measured at different GdmCl concentrations

	0.5 M	**0.65 M**	**0.75 M**	**0.85M**	**1M**
Number of trajectories	761	1333	1810	1969	1299
Average trajectory length before photobleaching step (seconds)	5.72	4.28	3.54	3.26	3.45
Total number of transitions determined by the HMM analysis	1359	1596	1983	2280	1212
Average number of transitions per trajectory	1.79	1.20	1.10	1.16	0.93

Table S2. The ten most abundant unfolding pathways as a function of GdmCl concentration

GdmCl concentration	Pathway	Probability %
0.5 M	5 → 1	16.6
	5 → 4 → 1	16.2
	5 → 3 → 1	11.5
	5 → 3 → 2 → 1	10.6
	5 → 2 → 1	10.1
	5 → 4 → 3 → 2 → 1	8.4
	5 → 4 → 3 → 1	8.1
	5 → 4 → 2 → 1	2.1
	5 → 6 → 1	2
	5 → 6 → 4 → 1	1.7
0.65 M	5 → 4 → 3 → 2 → 1	18.7
	5 → 3 → 2 → 1	15.7
	5 → 4 → 3 → 1	11.5
	5 → 1	11
	5 → 3 → 1	9.8
	5 → 6 → 3 → 2 → 1	5.2
	5 → 6 → 4 → 3 → 2 → 1	3.8
	5 → 2 → 1	3.5
	5 → 6 → 3 → 1	3.4
	5 → 4 → 1	3.4
0.75 M	5 → 4 → 3 → 2 → 1	31.4
	5 → 4 → 3 → 1	14.2
	5 → 3 → 2 → 1	10.7
	5 → 4 → 2 → 1	5.2
	5 → 3 → 1	4.9
	5 → 4 → 1	4.3
	5 → 6 → 3 → 2 → 1	4.1
	5 → 2 → 1	4
	5 → 6 → 2 → 1	3.8
	5 → 1	3.7
0.85 M	5 → 4 → 3 → 2 → 1	20.4
	5 → 2 → 1	12.8
	5 → 3 → 2 → 1	10.3
	5 → 4 → 3 → 1	9.7
	5 → 4 → 2 → 1	9.5
	5 → 3 → 1	5.3
	5 → 6 → 2 → 1	5.1
	5 → 6 → 3 → 2 → 1	4.7
	5 → 1	3.5
	5 → 4 → 1	3.3

1 M	5 → 4 → 3 → 2 → 1	48.5
	5 → 2 → 1	14
	5 → 4 → 3 → 1	8.8
	5 → 4 → 2 → 1	6.8
	5 → 6 → 2 → 1	4.4
	5 → 1	4.3
	5 → 3 → 2 → 1	3.9
	5 → 6 → 3 → 2 → 1	3.3
	5 → 3 → 1	0.9
	5 → 4 → 3 → 6 → 2 → 1	0.8

Unfolding pathways were obtained by applying the transition-path theory of Weikl and coworkers [44] or, equivalently, a stochastic simulation to the HMM model transition probability matrices. In the simulation, 10,000 trajectories were generated in state space starting from the folded state (state 5), and ending when reaching state 1. It is important to note that dynamics on multiple-state landscapes might involve back-and-forth jumps, which lead to loops in pathways, e.g. $\ldots i \rightarrow j \rightarrow k \rightarrow j \rightarrow l \ldots$. Obviously, loops carry neither forward nor backward flux, and they were therefore removed from the trajectories, and pathways of each type were then enumerated. The ten most abundant pathways obtained by both methods are shown in the table.

Table S3. Transition probability matrix from the HMM analysis of the 0.65 M GdmCl data set

To / From	1	2	3	4	5	6	Bleached state
1	9.4E-01	2.2E-02	9.8E-03	1.1E-03	1.2E-03	4.1E-04	2.2E-02
2	1.1E-02	9.5E-01	2.7E-02	4.9E-04	3.6E-04	2.5E-04	1.5E-02
3	2.9E-03	1.6E-02	9.5E-01	6.9E-03	1.3E-03	1.1E-03	1.8E-02
4	1.2E-03	1.0E-03	2.5E-02	9.5E-01	8.5E-03	4.6E-03	9.5E-03
5	7.1E-04	4.2E-04	2.6E-03	4.7E-03	9.8E-01	3.6E-03	4.3E-03
6	4.1E-04	4.9E-04	3.8E-03	4.3E-03	6.1E-03	9.8E-01	3.5E-03
Bleached state	0	0	0	0	0	0	1

Numbers in this table represent the probabilities for transitions between pairs of states to occur in 50 ms, as obtained from the 0.65 M GdmCl data set using the HMM analysis. The transition probabilities from the bleached state back to any of the 'real' states are by definition 0.

Table S4. Change-point and HMM analysis of a simulated data set

Method	**Missed sequential transitions**	**Missed non-sequential transitions**	**Total number of false positive identifications**
HMM	1.7 %	2 %	236
Change point, CS	39 %	21 %	578
Change point, MSE	37 %	22 %	549

The table shows results of analysis of simulated data using the two change point methods and the HMM. For details see the section "**Tests of methods for detection of transitions**" in the Supplementary methods.

Table S5. Assessment of HMM analysis of the 0.65 M GdmCl data set - FRET efficiency values

State	Mean FRET efficiency values from original HMM analysis	Standard deviation	FRET efficiency values from analysis with 100 ms bins	FRET efficiency values from analysis with 150 ms bins
1	0.1172	0.0016	0.1255	0.1258
2	0.2675	0.0026	0.2768	0.2688
3	0.4049	0.0014	0.4080	0.3998
4	0.6006	0.0009	0.5921	0.5890
5	0.7473	0.0006	0.7457	0.7460
6	0.8315	0.0016	0.8325	0.8323

Standard deviation values were estimated using bootstrapping. For details on this analysis see the section "**Assessment of the robustness of the HMM data analysis**" in the Supplementary Methods.

Table S6. Assessment of HMM analysis of the 0.65 M GdmCl data set- State propensities

State:	State propensity values from original HMM analysis	Standard deviation	State propensity values from analysis with 100 ms bins	State propensity values from analysis with 150 ms bins
1	0.0990	0.0075	0.1086	0.1040
2	0.2002	0.0279	0.2157	0.2008
3	0.3374	0.0274	0.3112	0.3258
4	0.0946	0.0086	0.0891	0.0912
5	0.1691	0.0118	0.1767	0.1842
6	0.0998	0.0096	0.0987	0.0941

Standard deviation values were estimated using bootstrapping. For details on this analysis see the section "**Assessment of the robustness of the HMM data analysis**" in the Supplementary Methods.

Table S7. Assessment of HMM analysis of the 0.65 M GdmCl data set-productive flux values

Transition type:	Relative productive flux values from original HMM analysis	Standard deviation	Relative productive flux values from analysis with 100 ms bins	Relative productive flux values from analysis with 150 ms bins
1→2	0.5130	0.0877	0.6221	0.5762
1→3	0.3005	0.0989	0.2925	0.3207
1→4	0.0524	0.0182	0.0217	0.0354
1→5	0.1101	0.0136	0.0548	0.0649
2→3	0.4235	0.0913	0.4869	0.4649
2→4	0.0223	0.0352	0.0593	0.040
2→5	0.0494	0.0136	0.0692	0.0633
3→4	0.3509	0.0425	0.3571	0.3595
3→5	0.2679	0.0210	0.3089	0.3538
4→5	0.3693	0.0147	0.3089	0.3538

Standard deviation values were estimated using bootstrapping. For details on this analysis see the section "**Assessment of the robustness of the HMM data analysis**" in the Supplementary Methods.

Supplementary Methods

Protein expression and labeling. The pEAK90 expression vector containing the *E. coli* AK C77S gene was a generous gift from the lab of Prof. Elisha Haas (Bar-Ilan University). Two alanine-to-cysteine substitutions were introduced at positions 73 and 203 of the protein by site-directed mutagenesis (using the StrataGene QuickChange kit). These sites were chosen to report on the folding dynamics of the CORE domain of AK. Previous studies showed that cysteine residues introduced at these two positions differ significantly in their labeling rates [48], which we exploited in order to selectively label each cysteine with a particular dye. The sequences of both AK C77S and three mutants - AK/C77S/A73C (AK73), AK/C77S/A203C (AK203), and AK C77S/A203C/A73C - were verified by DNA sequencing. Each mutant was over-expressed, using published methods [33], in transformed *E. coli*. DH5α cells. The cells were lysed, and the lysate was separated on a DEAE ion-exchange column (GE Healthcare DEAE HiTrap FF). Fractions containing AK were pooled and run on a second gel filtration column (GE Healthcare HiLoad 16/60 Superdex 75 prep grade). AK eluted as a single peak and was concentrated and stored in 50% glycerol at -20°C. Purity was tested on an SDS-PAGE and found to be >95%. MALDI mass-spectrometry was used to assess the purity of the sample and to verify the molecular weight of the protein. Enzymatic activity of the various mutants was checked and found to conform to reported values.

Labeling reactions were preceded by incubation of the protein samples in a freshly prepared 1mM solution of DTT. The DTT was then removed using a Bio-Rad Micro Bio-Spin 6 size exclusion column. AK73 and AK203 were labeled with either Alexa 488 maleimide (Invitrogen) or ATTO 590 maleimide (ATTO-TEC) following standard procedures, and were separated on a mono-Q 5/50 GL column (GE Healthcare). AK73 labeled with Alexa 488 was found to elute at a different ionic strength than AK203 labeled with Alexa 488, which facilitated separation of the double labeled protein with the desired dye configuration (C73 Alexa 488, C203 ATTO-590) on a mono-Q column. Double labeling proceeded in two steps in degassed phosphate buffer saline (PBS): We first labeled with ATTO 590 maleimide, which preferentially reacted with C203, and then with Alexa 488 maleimide. The second step was performed in a buffer containing 2M GdmCl. Excess dye molecules

were separated using a size exclusion spin column (as above), and the protein was refolded by slow dialysis into 50mM Tris pH 8.0 following the procedure described by Ratner et al. [49]. The various labeled species were separated on a mono-Q column.

We performed temperature-dependent CD measurements on a Jasco J-815 spectrometer in order to assess the change in stability of the protein upon double labeling (a comparison based on GdmCl denaturation would require prohibitively large protein quantities). Based on the CD signal at 222 nm, it was found that the transition temperature of the unlabeled protein was 41.9 ºC, while that of the double-labeled protein was 39.0 ºC.

Steady-state measurements. Ensemble/bulk fluorescence studies were conducted on a Fluorolog spectrofluorometer (Jobin-Yvon) equipped with Glan-Thompson polarizers. AK73 labeled with Alexa 488, and the double-labeled AK73-203 were used for control experiments, including evaluation of fluorescence quantum yield and anisotropy values as a function of GdmCl concentration (Control). AK73-203 was also used for measuring the ensemble/bulk denaturation curve. The concentration of each GdmCl stock solution was determined using a Fisher Abbe refractometer (Fisher Scientific Co.).

Sample preparation for single-molecule experiments. Liposomes made of egg phosphatidylcholine and a fraction of 1:500 of 1,2-dioleoyl-sn-glycero-3-phosphoethanolamine-N-(cap biotinyl) (both from Avanti Lipids) were prepared by extrusion [34] in the appropriate buffer, using a disposable 0.1 μm Anopore syringe filter (Whatman Anotop-10). To prepare protein-loaded liposomes, we added labeled protein to a final concentration of ~0.3 μM, chosen so that one out of ~10 liposomes will contain a single molecule [35]. Liposomes were separated from non-encapsulated protein on a size exclusion column (GE Healthcare MicroSpin S-400 HR).

Sample cells were made of two glass #1.5 coverslips (Thomas Scientific), which were glued together with two Teflon strips. A supported lipid bilayer was formed on the glass surfaces by incubating a cell with a solution containing empty liposomes. Incubation with a solution of 1 mg/ml streptavidin (Sigma) was followed by introduction of protein-loaded liposomes into the cell. Finally, to prevent buffer evaporation during measurement, the cell was sealed with silicon grease.

Single-molecule setup and data acquisition. A custom-made single-molecule microscope for automated data collection was constructed. A scheme of the system is shown in Figure S1, and the labels of the various parts in the figure are included in the detailed description below. The beam of an argon ion laser (Spectra-Physics model 163, 488nm) was passed through a laser-line cleanup filter (designated LP in the figure, Chroma Z488/10x) and expanded five times (BX) to fill the back aperture of a 100x oil-immersion objective (OBJ, Zeiss FLUAR 100x/1.3NA). A sample cell (SAM) was mounted on a custom-designed sample holder on top of a capacitance-feedback 100x100x20μm piezo stage (PIEZO, PI P-517) controlled by a dedicated digital signal processor (PI E-710). The piezo stage was mounted on top of a coarse motorized stage (MS) to allow larger-scale motion of the sample. The sample was excited by the focused laser beam and fluorescent emission from the sample was collected by the objective, passed through the first dichroic mirror (DIC1, Chroma 505DCLP), filtered from remaining excitation light (EF, Semrock LP02-488RU), and split into two detection channels by a second dichroic mirror (DIC2, Chroma 565DCLP). The donor dye emission and acceptor dye emission were filtered by respective emission filters (DF, Semrock FF01-536/40 and AF, Semrock FF01-624/40) and focused onto two single-photon avalanche photo-diodes (APD, Perkin-Elmer SPCM-AQR-15). The arrival times of individual photons to the APDs was recorded by a counter/timer card (National Instruments NI6602) with time resolution of 12.5 ns. A standalone TCSPC module (PicoHarp 300, PicoQuant) was used in place of the counter/timer card in free diffusion experiments. To prevent excess illumination of the sample, a mechanical shutter (ST, Uniblitz LS6T2) blocked the laser when measurements were not in progress.

In order to generate an auto-focus mechanism, laser light that was back-reflected from the sample surface was focused on a pinhole (PH) and measured by a photomultiplier tube (PMT, Hamamatsu H8249). The PMT position was adjusted to register maximal photon flux when the sample was exactly at the microscope focus. The piezo stage was scanned in the z direction periodically to find the focused position.

Data acquisition was fully automated using dedicated software programmed in LabWindows/CVI and MATLAB. A 5 μm x 5 μm region of the sample was scanned, and the position of vesicles loaded with molecules was identified with subpixel

resolution. The piezo stage was used to position the laser beam on each of these in turn, in order to obtain a fluorescence time trace (trajectory). For each vesicle, both donor and acceptor signals were recorded for one minute, or until the background level was reached. After acquiring trajectories of all molecules in a field, the piezo stage was moved to a new region, the focus position was adjusted and the acquisition cycle was repeated. The laser power was set to 1000 nW during the scan and 250 nW during time-trace acquisition.

Free-diffusion experiments. Cells filled with a dilute solution (15 pM) of AK molecules at a particular denaturant concentration were used for these experiments. The surfaces of these cells were covered with a supported bilayer, and the solution contained 0.01% Tween, both included in order to minimize protein adsorption. The laser beam was focused 14 μm into the solution, and data was collected continuously for 1 hour before the sample was replaced. Several such data sets were collected at each denaturant concentration. Detection of photon bursts and their analysis were performed as described previously [50].

Control experiments. A series of control experiments was conducted in order to ensure the high quality of the collected data and discard possible artifacts. The first four of these control experiments allowed us to conclude that the Förster distance of the donor-acceptor pair does not change as the GdmCl concentration is varied, and by implication also that the Förster distance is not state-dependent.

- We confirmed that emission spectra of the labeled proteins did not change due to local environment variations following increasing denaturant concentrations. To this end, the emission spectra of the donor and acceptor dyes on the protein were measured as a function of GdmCl concentration. For the donor spectra we used molecules labeled with the donor dye only, excited at 465 nm. For acceptor spectra we used double-labeled protein molecules, excited at 560 nm. Shifts larger than 1 nm were not observed in the spectra.

- We confirmed that the quantum yield of the acceptor dye was unaffected by the denaturant by measuring the emission spectra of double-labeled protein

molecules excited at 560 nm as a function of GdmCl concentration, and integrating the spectra (Figure S2).

- We verified that the donor quantum yield did not change as the concentration of GdmCl increased, directly using the double-labeled protein sample. To that end, we measured emission spectra of the double-labeled protein following excitation at 465 nm, as a function of GdmCl concentration. We then calculated the γ-corrected total emission intensity defined as $I(\gamma) = \gamma \int I_{DD}(\lambda) d\lambda + \int I_{AD}(\lambda) d\lambda$, where $I_{DD}(\lambda)$ and $I_{AD}(\lambda)$ are the donor and acceptor contributions to the emission spectrum. γ corrects for differences in quantum yields of the two dyes and in detection efficiencies in the spectral ranges of $I_{DD}(\lambda)$ and $I_{AD}(\lambda)$. The donor contribution was calculated by subtracting the proportional acceptor emission spectrum from the total emission spectrum. Since we already showed above that the acceptor is not sensitive to GdmCl concentration, the γ-corrected total emission intensity should also be independent of GdmCl if the donor is not affected by the denaturant. Figure S3 shows that this is indeed that case.

- The bulk fluorescence anisotropy of the dyes on the protein was measured at different GdmCl concentrations (Figure S4). The low values of the fluorescence anisotropy, and the minimal changes induced by GdmCl, indicate that the dyes are free to reorient, independently of the denaturant concentration. According to the work of Haas et al. [51], the measured anisotropies of the dyes can lead to ~10% uncertainty in distance determinations, but since we do not attempt to convert the FRET values to distances, this is of less importance to our current work.

- Finally, Chung et al observed photo-induced changes of the emission spectra of individual Alexa-488 molecules [23]. We explicitly showed that such changes are not significant under the conditions of our experiment using the following experiment. Individual molecules of AK73 labeled with Alexa-488 (donor-only-protein) were encapsulated in vesicles and intensity trajectories were obtained using our single-molecule setup. For this experiment emission filters were selected to allow an increased leak to the “acceptor channel” (20% as

opposed to the standard 7%). Any significant change in the emission spectrum of the dye should have resulted in anti-correlated changes in the intensities of the two detectors. Among ~4500 measured trajectories, we found changes that can be categorized as anti-correlated transitions in less than 1%, indicating that photo-induced changes in the donor spectrum can be neglected.

Initial treatment of measured trajectories. The following steps were taken in the treatment of single-molecule trajectories before analysis, in order to ensure their quality and prevent artifacts. These steps were implemented automatically, and resulted in selection of 7-10% of the trajectories (depending on the data set) for further analysis.

- First, since the time between folding/unfolding transitions in AK is long (of the order of 1 second), we binned the two data sets in each trajectory (donor and acceptor) in 50 ms time windows to get $I_{D,raw}(t)$ and $I_{A,raw}(t)$.

- We used change point analysis (see below) to identify trajectories that did not show a photobleaching step, and removed them from the set.

- The lowest intensity region in each single-molecule trajectory (required to be longer than 1 second) was identified as the background level for that molecule. Trajectories with a total background level larger than 400 cps, or individual channel background levels (b_D, b_A) larger than 200 cps, were removed.

- Any trajectory with a total intensity larger than 1600 was also removed, as it might have arisen from two molecules in the same or nearby vesicles.

- The intensity of the remaining trajectories was then corrected for background and leakage of photons from donor to acceptor channel using:

$$I_D(t) = \left(I_{D,raw}(t) - b_D\right)(1+\lambda)$$
$$I_A(t) = \left(I_{A,raw}(t) - b_A\right) - \lambda\left(I_{D,raw}(t) - b_D\right)$$

with the leakage factor λ = 0.069 measured using a solution of free Alexa-488 molecules (we verified that the spectral properties of the donor-labeled protein are essentially identical to those of the free dye).

- To ensure that essentially only anti-correlated intensity changes in donor and acceptor occur in the trajectories (as expected for FRET transitions), we cut the trajectories whenever the total intensity ($= I_D(t) + I_A(t)$) changed by more than 25%. In most cases, this point occurred when the donor photobleached, although in some trajectories we identified additional intensity changes.

- We also made sure that the acceptor data set of each trajectory included a photobleaching step (which could occur either simultaneously with the donor photobleaching step or independently of it). Trajectories that did not show such a photobleaching step were discarded.

- Finally, the FRET efficiency was calculated as $\varepsilon(t) = I_A(t)/(I_A(t) + \gamma \cdot I_D(t))$ for the remaining molecules. γ in this expression corrects for the difference in quantum yields of the two dyes and detection efficiencies of the two channels in our setup. We obtained γ by comparing the total intensities before and after the acceptor photobleaching step in a set of selected single-molecule trajectories. For the two dyes used in this work and with our current optical design we found that γ is ~1.

Change-point analysis. Single-molecule trajectories collected in this study exhibited sharp transitions between intensity levels and/or FRET efficiency levels. To identify transitions in these signals we implemented a model-free change-point analysis algorithm, which has the large advantage in that it does not require any prior knowledge on the underlying signal dynamics and noise statistics. Two different change-point analysis methods were used [52], with similar results (see discussion based on simulations below). The two methods are described below.

Change-point analysis, cumulative sum (CS) method. For a generic trajectory *s(t)*, the CS trajectory, $\tilde{s}_{CS}(t)$, is defined by $\tilde{s}_{CS}(t) = \sum_{t'=1}^{t} \left(s(t') - \langle s \rangle\right)$ where $\langle s \rangle$ is the time-average of *s(t)*. In the absence of any transition in the whole trajectory, the term in brackets is small and $\tilde{s}_{CS}(t)$ fluctuates around the zero value. If a transition from a low to a high mean value occurred at time *t*, $\tilde{s}_{CS}(t)$ will decrease before *t* and increase at later times. If the transition is from a high value to a low one, $\tilde{s}_{CS}(t)$ will first

increase and then decrease. The estimated transition point is therefore where $abs(\tilde{s}_{CS}(t))$ is maximal.

Change-point analysis, mean squared error (MSE) method. In this method each trajectory is split into two segments, the first running from $\tau=1$ to t and the second from $\tau=t+1$ to T, and the following function is calculated: $\tilde{s}_{MSE}(t)=\sum_{\tau=1}^{t}\left(s(\tau)-\langle s\rangle_1\right)^2+\sum_{t}^{T}\left(s(\tau)-\langle s\rangle_2\right)^2$ where $\langle s\rangle_1$ and $\langle s\rangle_2$ are the time-averages of the first and second segments, respectively. The value of t that minimizes $\tilde{s}_{MSE}(t)$ is the best estimator of the last point before the change.

To estimate the statistical significance of each transition point found by one of the above methods, we generated 10000 bootstrapped versions from each trajectory *s(t)*, and reanalyzed them with the change-point algorithm. We then calculated a weight according to $W=\max\left[\tilde{s}(t)\right]-\min\left[\tilde{s}(t)\right]$ for both the original trajectory and each of the 10000 bootstrapped versions. A transition was considered significant if W of the original trajectory exceeded W of >95% of the bootstrapped versions. To identify multiple transitions in the same trajectories, we used the above procedure iteratively with a running window of 50 bins. When the algorithm found a transition within a window, the next window started exactly after the location of this transition. Otherwise, the next window was positioned to have an 80% overlap with the previous one. The procedure was repeated in order to find a possible missed transition between each pair of detected transitions, until no further transitions were uncovered. After finding all putative transitions, we reevaluated the exact temporal position of each change point separately within its own segment by the same method.

Tests of methods for detection of transitions. To determine the efficiency and accuracy of the various methods for transition detection, we analyzed a set of 4000 simulated trajectories. The total number of transitions in the simulation was 12,040, out of which 6,268 were sequential ($i\rightarrow i\pm1$) and 5,772 were non-sequential ($i\rightarrow j$, where $j>i+1$ or $j<i-1$). The two change-point algorithms and the HMM algorithm were used to analyze the simulated data. The number of false positive transition identifications and missed sequential and non-sequential transitions for each analysis method is shown Table S4. The change-point analysis tends to miss a significantly

larger number of transitions than the HMM analysis, especially those of the sequential type (which are smaller). The number of spurious transitions found by all methods is relatively low.

We also used simulated trajectories to test the method for selection of the correct number of states in the HMM analysis. In *all tested cases*, it was found that cross-correlation of the transition density maps generated by change-point and HMM analyses identified the correct number of states. This shows that the fact that the change-point analysis misses a significant fraction of the transitions does not impede the correlation analysis from performing correctly. The reason for this is that failure to identify transitions by the change-point analysis is not state dependent, and depends only on the distance from the diagonal. Therefore, there is no significant distortion of the overall shape of the change-point map due to the missing transitions.

Assessment of the robustness of the HMM data analysis. To assess the accuracy of the HMM data analysis, we performed the following two tests on the 0.65 M data set, the results of which are reported in Tables S5-S7.

1. We repeated the analysis after binning the trajectories in 100 ms and 150 ms bins-see results in Tables S5-7.

2. We estimated parameter errors using a bootstrapping procedure. In particular, using the HMM optimal model parameters we generated 100 synthetic data sets. The number of simulated trajectories in each data set was the same as in our experimental one. However, the length of each trajectory was stochastically determined based on the photobleaching rates of the various states. We than ran the HMM analysis on each synthetic data set separately. In order to ensure convergence we ran 1000 HMM analyses for each synthetic data set, each analysis starting from a different random set of initial HMM parameters. Finally, we performed a productive flux analysis and calculated the deviations from the values obtained from the original experimental data. Standard deviations calculated from the bootstrapping analysis are reported in Tables S5-7.

Supplementary references

[48] Ratner, V., Kahana, E., Eichler, M., and Haas, E., *Bioconjugate Chem.* **13** (5), 1163 (2002).

[49] Ratner, V., Amir, D., Kahana, E., and Haas, E., *J. Mol. Biol.* **352** (3), 683 (2005).

[50] Sherman, E. and Haran, G., *Proc Natl Acad Sci U S A* **103** (31), 11539 (2006).

[51] Haas, E., Katchalski-Katzir, E., and Steinberg, I. Z., *Biochemistry* **17** (23), 5064 (1978).

[52] Taylor, W. A., Change-point analysis: A powerful new tool for detecting changes, Available at http://www.variation.com/cpa/tech/changepoint.html, (2000).